PROCEEDINGS A

royalsocietypublishing.org/journal/rspa

Research

Cite this article: Lucido M, Balaban MV, Nosich AI. 2022 Terahertz-range plasmon and whispering gallery mode resonances in the plane wave scattering from thin microsize dielectric disk with graphene covers. *Proc. R. Soc. A* **478**: 20220126.
https://doi.org/10.1098/rspa.2022.0126

Received: 16 March 2022
Accepted: 4 May 2022

Subject Areas:
electromagnetism, integral equations, computational mathematics

Keywords:
thin graphene–dielectric–graphene disk, scattering, absorption, integral equation, method of analytical preconditioning, resonances

Author for correspondence:
Mario Lucido
e-mail: lucido@unicas.it

Terahertz-range plasmon and whispering gallery mode resonances in the plane wave scattering from thin microsize dielectric disk with graphene covers

Mario Lucido[1], Mykhaylo V. Balaban[2] and Alexander I. Nosich[2]

[1]Department of Electrical and Information Engineering, University of Cassino and Southern Lazio, Cassino, Italy
[2]Laboratory of Micro and Nano Optics, Institute of Radio-Physics and Electronics NASU, Kharkiv, Ukraine

ML, 0000-0001-8661-5601

We analyse the scattering and absorption of a terahertz-range plane wave by a thin circular dielectric disk with two graphene covers. Assuming that the thickness of the whole composite disk is much smaller than the free-space wavelength, we reduce the complexity of the problem with the aid of the generalized boundary conditions. This yields a set of singular integral equations for the effective electric and magnetic currents, induced on an equivalent zero-thickness disk. The adopted advanced numerical solution technique is a version of the method of analytical preconditioning, which uses weighted polynomials as expansion functions in the discretization of the integral equations. Then, the resulting matrix equation has Fredholm second-kind property that enables us to control the computational error by the matrix size and reduce it to the desired level. This accurate analysis reveals resonances on several types of natural modes, best understood via visualization of in-resonance near-fields. They are the plasmon-mode resonances of the graphene disk, perturbed by the presence of the dielectric filler, and the dielectric disk modes, perturbed by the graphene covers. Additionally, quasi-full disk transparency is observed if the transverse resonance condition is

THE ROYAL SOCIETY PUBLISHING

fulfilled. Special attention is paid to the tunability of the found effects with the aid of graphene's chemical potential.

royalsocietypublishing.org/journal/rspa *Proc. R. Soc. A* **478**: 20220126

1. Introduction

The patterned graphene configurations are actively exploited in the ongoing research and development of innovative infrared and terahertz (THz) devices and systems [1–3]. This is because of two properties featured by graphene [4]: (i) its surface conductivity is very high and, moreover, tunable with the aid of a DC bias, which translates into graphene's chemical potential and (ii) the surface impedance of graphene (inverse to the conductivity) has an inductive imaginary part that leads to the existence of the moderate-lossy plasmon guided wave on an infinite sheet of graphene. On the finite-size graphene structures, the mentioned plasmon wave bounces between the sample edges and creates the standing waves, i.e. the natural plasmon modes. The resonance frequencies of these modes, as a result, are also tunable with the aid of a DC bias. The resonances on the graphene plasmon modes are actively studied today and have already found applications in the design of novel biosensors [5–7] and antennas [8] in the mid-infrared and THz ranges. The use of graphene, instead of the noble metals, in the design of plasmonic nanolasers is also actively discussed [9].

What is also important, the wavelength of the plasmon guided wave is much smaller than the free-space wavelength [4]. Therefore, the frequencies of the lowest plasmon modes on the finite samples of graphene are found in the sub-wavelength range relative to the free-space wavelength. Note also that the bulk losses in graphene and hence the attenuation constant of the plasmon guided wave is rather small—therefore, the plasmon natural modes have moderate Q-factors around 100 in the THz range and above that value in the infrared range. Additionally, although free-standing or suspended graphene is realizable and attracts the attention of researchers as more chemically stable [10], in most practical situations, graphene lies on dielectric substrates, which provide mechanical rigidity.

Despite rapid advances of nanotechnologies, the manufacturing of the patterned graphene configurations on dielectric or semiconductor substrates, using the chemical vapour deposition (CVD) and subsequent molecular-beam epitaxy processes, is still an expensive matter [11]. Therefore, a preceding computer modelling, if it is trusted, fast and accurate, is important as a tool of design that enables avoiding costly and time-consuming prototyping. Here, one can see a sort of permanent competition between the general-purpose commercial codes, which have relatively low accuracy and may suffer from the convergence troubles (see [12,13] for some reviews), and mathematically sophisticated advanced in-house algorithms [14]. The latter are superior in performance because of the guaranteed convergence and controlled accuracy to machine precision, however, are normally oriented to handle a narrower class of electromagnetic geometries. Additionally, commercial codes, especially those based on the finite-difference time-domain approach, entail huge numbers of unknowns and correspondingly enormous computation times even for simple mesoscale objects, if they are in the free space, and the radiation condition is satisfied only approximately. As mentioned in [14], all these numerical troubles can be completely eliminated with either of two especially advantageous approaches—the method of analytical regularization (MAR) and the Nystrom discretization of the associated singular integral equations (ND-SIEs) [15]. These convergent techniques exploit the fact that graphene is, actually, a zero-thickness resistive sheet with frequency-dependent resistivity (*resistivit*y is a short term substituting for the longer expression *complex electric surface resistance*; an equivalent term is *surface impedance*).

Among many possible forms of the patterned graphene, the most frequent are perhaps the straight strips and the circular disks, because of their simplicity. Therefore, it is no surprise that the scattering and absorption of infrared and THz waves by graphene strips and arrays of them has been a topic of numerous research papers—see, for instance, [16–19] and references

therein. The most reliable and accurate results have been computed using the MAR approach based on the static-part inversion [16,17] and the ND-SIEs [18,19] with Chebyshev quadratures. In a similar manner, the scattering and absorption by graphene disks and arrays of them has been treated using various approaches and techniques. The Purcell effect, i.e. modification of the elementary dipole radiation in the presence of graphene disk, was analysed with MAR in the Hankel transform domain in [20] and the plane wave scattering and absorption by such a disk was treated with analytical preconditioning of SIEs in [21]. Nystrom discretization can be also used if the perfectly electrically conducting (PEC)-disk algorithm of Bulygin *et al.* [22] is slightly modified to adapt to the resistive surface boundary conditions.

Still, as mentioned, in most realistic situations, graphene lays on finite-thickness dielectric substrates, which can bring additional effects such as guided waves, on infinite layers, and morphology-dependent natural modes and associated scattering resonances, on finite substrates. Although disks on infinite substrates are beyond our work, we can point out that they are accessible both with MAR and ND-SIEs if the free-space Green's function is replaced with the appropriate Green's function of the layered host medium. The latter functions are always known as Fourier–Hankel transforms of certain functions, the poles of which correspond to the guided waves. Along these lines, MAR analysis of the axially symmetric radiation of elementary dipoles above a resistive disk residing on a substrate was performed in [23].

The goal of our work is the accurate analysis of the resonance effects in the scattering and absorption of a THz-range plane electromagnetic wave, obliquely incident on the composite circular disk made of three different layers: graphene, dielectric and graphene, i.e. *GDG disk*. Under the assumption that the total thickness is much smaller than the free-space wavelength, such a 'sandwich pillbox' can be characterized using the generalized boundary conditions (GBC) [24,25]. GBC allow to eliminate the inner field and consider the disk as zero thickness. However, the latter value is still present: GBC involve two complex-valued resistivities, electric and magnetic, which depend on the optical thickness and material parameters of both dielectric and graphene [26].

In our analysis, we use the analytical–numerical MAR technique, earlier developed for single thin dielectric disk [27,28] and single graphene disk [21], in the free space. It is based on the derivation, using the GBC, of a set of SIEs for each azimuthal Fourier harmonic of the scattered field, where the unknown functions are the harmonics of the effective electric and magnetic currents on the disk. Then, these SIEs are projected on the sets of judiciously selected basis functions, which are related to certain Jacobi polynomials and serve as the orthogonal eigenfunctions of the most singular parts of SIEs. Such a projection, besides the discretization of SIEs, enables analytical inversion of their most singular parts and casts the SIEs to the Fredholm second kind infinite-matrix equations. Therefore, this technique is also called the method of analytical preconditioning (MAP). The latter equations can be truncated and solved numerically, with their convergence guaranteed by the Fredholm theorems and the accuracy controlled by the truncation order.

As the SIEs for the GDG disk differ only by the effective resistivities, adapted to account for the sandwich structure, and the MAP procedure remains the same, here we skip the details and instead cite the corresponding equations of [28]. Note that we use the time dependence as $\exp(+j\omega t)$, where ω is the cyclic frequency, which is omitted.

2. Formulation and solution method

In figure 1, a GDG disk, i.e. a homogeneous and isotropic dielectric disk covered by two monolayer graphene disks, one for each side, and located in the free space, is sketched. A Cartesian coordinate system, (x, y, z), and a cylindrical coordinate system, (ρ, ϕ, z), are introduced so that the z-axis coincides with the disk axis and the median surface S of the GDG disk is located at the abscissa $z = 0$. The notations a, τ, ε_0, μ_0, ε_r, μ_r, σ_s stand for, respectively, the disk radius, the disk thickness, the free space dielectric permittivity and magnetic permeability, the relative dielectric permittivity and the relative magnetic permeability of the dielectric

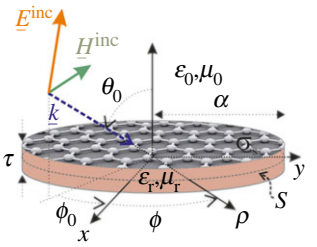

Figure 1. Geometry and notations for the arbitrary plane wave scattering from a thin dielectric disk with graphene covers. (Online version in colour.)

material, and the graphene surface conductivity. Henceforth, the symbols, λ, $k_0 = 2\pi/\lambda = \omega\sqrt{\varepsilon_0\mu_0}$ and $Z_0 = \sqrt{\mu_0/\varepsilon_0}$ will be used to denote the free-space wavelength, wavenumber and impedance, respectively. A scattered field is generated by the impinging plane wave sketched in figure 1, where $\underline{E}^{\mathrm{inc}}(\underline{r}) = \underline{E}_0 \mathrm{e}^{-\mathrm{j}\underline{k}\cdot\underline{r}}$, $\underline{H}^{\mathrm{inc}}(\underline{r}) = (Z_0 k_0)^{-1}\underline{k} \times \underline{E}_0 \mathrm{e}^{-\mathrm{j}\underline{k}\cdot\underline{r}}$, $\underline{r} = (\rho, \phi, z)$ and $\underline{k} = -k_0(\sin\theta_0 \cos(\phi_0 - \phi)\hat{\rho} + \sin\theta_0 \sin(\phi_0 - \phi)\hat{\phi} + \cos\theta_0 \hat{z})$, so that the total field, $\{\underline{E}(\underline{r}), \underline{H}(\underline{r})\}$, is given by the sum of the incident field and the scattered field.

Supposing that $\tau \ll a$ and $\tau \ll \lambda$, the field inside the dielectric disk can be neglected and the finite-thickness disk itself approximated with a zero-thickness disk located at the median surface S. The latter disk can be interpreted as a finite part of a generalized imperfect surface characterized with suitable complex surface resistances, or simply *resistivities* [24]. Just as an example, for $\mu_r = 1$, and for a high-contrast dielectric material, i.e. $|\varepsilon_r| \gg 1$, or for normal incidence of the plane wave, the electric and magnetic resistivities of a thin dielectric slab are found as [24],

$$R'_{\mathrm{e}} = -\mathrm{j}\frac{Z_0}{\sqrt{\varepsilon_r}} \cot\left(\frac{1}{2}k_0\tau\sqrt{\varepsilon_r}\right) \tag{2.1a}$$

and

$$R'_{\mathrm{m}} = -\mathrm{j}\frac{\sqrt{\varepsilon_r}}{Z_0} \cot\left(\frac{1}{2}k_0\tau\sqrt{\varepsilon_r}\right). \tag{2.1b}$$

These values serve as coefficients in GBC, which have to be imposed on the zero-thickness layer when neglecting the inner domain of the slab and the associated inner electromagnetic field. Besides, in the analysis of the scattering from finite-radius disk, these GBC (derived for the infinite dielectric slab) have to be supplemented with a condition that limits the singularity of the field at the disk's sharp rim. Such a condition is known to be the finiteness of the field power in the local sense, i.e. in any finite domain containing the rim.

On the other hand, the monolayer graphene disk can be seen as a finite resistive surface characterized with a complex surface resistivity or surface impedance, which, in turn, is the inverse of the graphene surface conductivity. Assuming that $a \geq 50$ nm, the edge effects on the graphene surface conductivity can be neglected. Indeed, it has been experimentally demonstrated that those effects only appear in structures with lateral dimensions considerably smaller than 100 nm [29]. Moreover, supposing that there is no magnetic bias field, the graphene can be assumed to be isotropic in the THz range due to the small with respect to the wavelength characteristic size of the honeycomb lattice nanostructure (10 nm). Taking into account that interband effects, in conductivity, can be neglected at all the frequencies below the visible light, the graphene surface conductivity can be expressed as a function of the cyclic frequency and the relaxation time (t_{relax}) by means of the Kubo formalism [4],

$$\sigma_{\mathrm{s}} = \frac{\Omega}{\mathrm{j}\omega + t_{\mathrm{relax}}^{-1}} \tag{2.2}$$

where

$$\Omega = \frac{q_e^2 c_B T}{\pi \hbar^2} \left\{ \frac{\mu_c}{c_B T} + 2\ln\left[1 + \exp\left(-\frac{\mu_c}{c_B T}\right)\right]\right\}. \tag{2.3}$$

In equation (2.3), q_e is the electron charge, c_B is the Boltzmann constant, T is the temperature, $\hbar$ is the reduced Planck constant and μ_c is the chemical potential. The corresponding graphene's electric resistivity or surface impedance is

$$R_e'' = \frac{1}{\sigma_s} = \mathrm{j}\frac{\omega}{\Omega} + \frac{1}{t_{relax}\Omega}. \tag{2.4}$$

As a result, the GDG disk can be interpreted as the superposition of three zero-thickness disks located at the plane $z = 0$. Hence, according to Bleszynski *et al.* [24], the total electric and magnetic fields have to satisfy the following GBC on S:

$$\frac{1}{2}\hat{z} \times (\underline{E}(\rho, \phi, 0^+) + \underline{E}(\rho, \phi, 0^-)) \times \hat{z} = R_e \underline{J}_e(\rho, \phi) \tag{2.5a}$$

and

$$\frac{1}{2}\hat{z} \times (\underline{H}(\rho, \phi, 0^+) + \underline{H}(\rho, \phi, 0^-)) \times \hat{z} = R_m \underline{J}_m(\rho, \phi), \tag{2.5b}$$

where the effective electric current density, $\underline{J}_e(\cdot, \cdot)$, and the effective magnetic current density, $\underline{J}_m(\cdot, \cdot)$, are defined as the jumps across S of the tangential components of the magnetic and electric fields to the GDG disk surface, respectively. Based on the strategy developed in [26], which allows to simply combine the resistive BC on the graphene monolayer with GBC on the zero-thickness dielectric substrate into a new set of effective GBC, it is possible to establish the following expressions for the effective electric and magnetic resistivities of the GDG disk, respectively:

$$R_e = \frac{R_e'}{1 + 2R_e'/R_e''} \tag{2.6a}$$

and

$$R_m = \frac{1}{2R_e''} + R_m' \tag{2.6b}$$

In figure 2, we demonstrate the frequency dependences of the real and imaginary parts of the graphene surface impedance, R_e'', and the electric and magnetic resistivities of the composite GDG structure, R_e and R_m. The graphene parameters are $T = 300\,\mathrm{K}$, $t_{relax} = 1\,\mathrm{ps}$, and $\mu_c = 0.1, 1, 10\,\mathrm{eV}$ while the relative dielectric permittivity and dielectric thickness are, respectively, $\varepsilon_r = 12(1 - \mathrm{j}10^{-5})$ and $\tau = 2\,\mu\mathrm{m}$.

As can be seen, the electric resistivity of the composite GDG structure features a remarkable peak of the real part and a double extremum of the imaginary part at the same frequency, controlled by the chemical potential. If the potential gets larger, then this frequency tends to the natural frequency of the lowest transverse resonance of the flat infinite slab of the same thickness and permittivity sandwiched by PEC planes; at this frequency, $\tau \approx \lambda/\left(2\sqrt{|\varepsilon_r|}\right)$. The corresponding natural mode can be called the slab mode and denoted by the symbol S_0; excitation of this mode entails quasi-full transparency of the slab. Note that such a tunable transparency of a GDG sandwich cylindrical parabolic reflector, illuminated by the E-polarized plane wave, was recently found in [30].

Therefore, we have a boundary value problem for the Maxwell equations, which is still three dimensions, however, simpler than the original problem for a finite-thickness disk. The cost of this simplification is clear: after such a replacement, we lose the information of the fine details at the rim of the original disk. Nevertheless, this problem admits a unique solution provided that the boundary conditions, local power finiteness condition and Silver–Muller radiation condition are satisfied [14,31]. According to the second Green's formula, since the scattered electric and magnetic fields can be expressed as the convolution of the effective electric and magnetic current densities, respectively, with Green's functions and their normal to the disk derivatives, the equations (2.5*a*) and (2.5*b*) can be interpreted as two decoupled surface integral equations for the

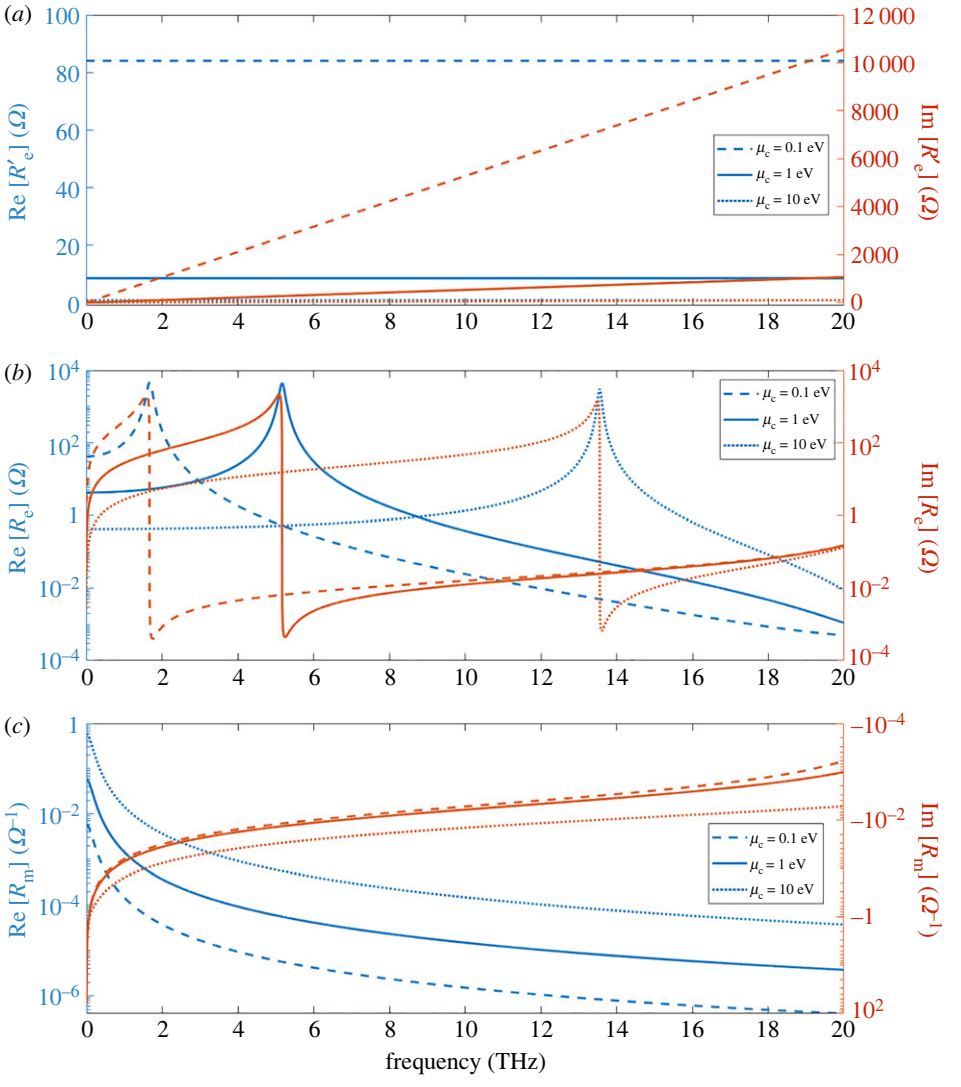

Figure 2. Frequency dependences of the real and imaginary parts of the graphene surface impedance (*a*), and the electric (*b*) and magnetic (*c*) resistivities of the GDG composite for $\varepsilon_r = 12(1 - j10^{-5})$, $\mu_r = 1$, $\tau = 2$ µm, $T = 300$ K, $t_{relax} = 1$ ps and $\mu_c = 0.1, 1, 10$ eV. (Online version in colour.)

effective current densities [24]. The revolution symmetry of the problem allows to reduce such equations to two infinite sets of independent one-dimensional integral equations in the Hankel transform domain for the spectral domain counterpart of the azimuthal harmonics of the effective current densities [32].

It is well known that no closed-form solutions for the obtained integral equations are available, hence, a discretization scheme has to be adopted to search for an approximate solution of the problem at hand. We apply a MAP discretization scheme, which is based on the Helmholtz–Galerkin technique developed in [21,27,28,33–35]. New unknowns are assumed according to the Helmholtz decomposition [36]: the surface curl-free contribution and the surface divergence-free contribution of the general harmonic of each effective current density. Suitable sets of orthonormal eigenfunctions of the most singular part of the integral operator, reconstructing the behaviour of the general harmonic of the currents at the disk rim and around the centre of the disk and admitting a closed-form spectral domain counterpart, are adopted to expand the unknowns in the

spatial domain [21,27,28,33–35]. In this way, the diagonalization of the most singular part of the integral operator immediately follows from the Galerkin projection. Moreover, the remaining part of the discretized operator is a compact operator in l^2 and the free term has a bounded l^2-norm, thus leading to a Fredholm second-kind matrix operator equation, i.e.

$$\boldsymbol{X}_r^{(n)} + \boldsymbol{A}_r^{(n)} \boldsymbol{X}_r^{(n)} = \boldsymbol{B}_r^{(n)}, \tag{2.7}$$

where $r = \mathrm{e}, \mathrm{m}$, $\boldsymbol{X}_r^{(n)}$ is the vector of the unknown expansion coefficients of the nth harmonic of the effective electric/magnetic current density, the elements of the compact matrix operator $\boldsymbol{A}_r^{(n)}$ differs from the ones in [28] only for the expression of the electric and magnetic resistivities and $\boldsymbol{B}_r^{(n)}$ is the free-term vector defined in [28]. Moreover, the elements of the matrix $\boldsymbol{A}_r^{(n)}$, which are one-dimensional improper integrals involving the products of Bessel functions of the first kind, are accurately and efficiently evaluated thanks to analytical techniques specifically developed in [34,35]. Hence, the convergence of the approximate solution, obtained by means of the truncation of the matrix equation, to the exact solution of the problem, is guaranteed. As will be shown later, the convergence is even fast because the selected expansion functions reconstruct the expected physical behaviour of the fields. It is worth observing that the computations relating to equation (2.7) may be readily reproduced by the reader by using the expressions and formulae explicitly provided in Appendix A of [28]. Indeed, these formulae may be coded straightforwardly in a MATLAB environment or similar, needing only a quadrature routine, evaluation of Bessel functions and a standard matrix equation solver, recognizing that the equations are well conditioned and not of large order. Other computations such as far-field patterns and postprocessing are completely standard and straightforward: the closed-form expressions for the absorption cross-section (ACS), total scattering cross-section (TSCS) and related quantities are available in [28] and are simple to implement.

3. Numerical results

(a) Convergence and validation

The aim of this section is to show the efficiency of the proposed method in the characterization of the physical properties of a GDG disk with $\tau \ll a$ and $\tau \ll \lambda$. Henceforth, we will implicitly assume $\mu_\mathrm{r} = 1$, $a = 50\,\mu\mathrm{m}$, $\tau = 0.04a$, $T = 300\,\mathrm{K}$ and $t_{\mathrm{relax}} = 1\,\mathrm{ps}$.

It is worth remembering that, by virtue of Fredholm theory, the convergence of the proposed method is guaranteed, i.e. the approximate solution obtained by truncating the matrix equation (2.7) tends to the exact solution of the problem as the truncation order tends to infinity. Now, we want to visualize the convergence and introduce the following relative computation error:

$$\mathrm{err}_{\mathrm{r},N}(M) = \sqrt{\frac{\sum_{n=-N+1}^{N-1} \left|\left|\boldsymbol{x}_{r,M+1}^{(n)} - \boldsymbol{x}_{r,M}^{(n)}\right|\right|^2}{\sum_{n=-N+1}^{N-1} \left|\left|\boldsymbol{x}_{r,M}^{(n)}\right|\right|^2}}, \tag{3.1}$$

where $2N-1$ is the number of the considered azimuthal harmonics estimated as in [37], $||\cdot||$ is the usual Euclidean norm and $\boldsymbol{x}_{r,M}^{(n)}$ is the vector of the expansion coefficients of the nth harmonic of the effective electric/magnetic current density evaluated by using M expansion functions for each unknown. It is worth noting, even if well known to the scientific community, that the error in (3.1), which is related to the currents' reconstruction, is of the order of magnitude larger than the relative computation error defined on the far-field. As mentioned in the previous section, once the currents are reconstructed, the far-field, the ACS, the bistatic radar cross section and the TSCS can be simply evaluated by means of closed-form expressions [28].

In figure 3, the behaviour of the relative computation error for the GDG disk with $\varepsilon_\mathrm{r} = 12(1 - \mathrm{j}10^{-5})$ and $\mu_\mathrm{c} = 1\,\mathrm{eV}$ is plotted for varying values of M and three operating frequencies (1, 5, 10 THz). Even if the analytical-numerical technique proposed in this paper works independently of the plane wave incidence angle and polarization, we concentrate on some

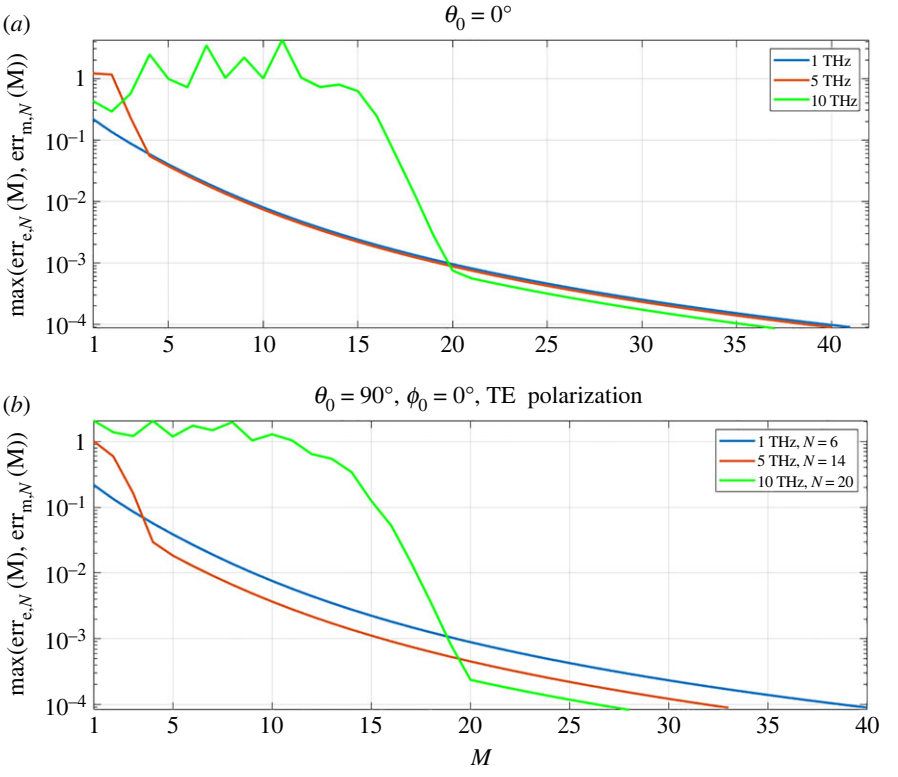

Figure 3. Relative computation error for the GDG disk with $\varepsilon_r = 12(1 - j10^{-5})$, $\mu_r = 1$, $a = 50$ µm, $\tau = 0.04a$, $T = 300$ K, $t_{relax} = 1$ ps, $\mu_c = 1$ eV versus M at $N = 6, 14, 20$ adapted to the three operating frequencies of 1, 5, 10 THz, respectively, for normal incidence ($\theta_0 = 0°$) (*a*) and grazing incidence ($\theta_0 = 90°$, $\phi_0 = 0°$) and TE polarization (*b*). (Online version in colour.)

cases avoiding others just for the sake of brevity. In figure 3*a*, the normal to the disk surface incidence plane wave is considered ($\theta_0 = 0°$). In such a case, only the harmonics for $n = \pm 1$ contribute to the field's representation. The convergence is really very fast as $M = 20$ allows to obtain $\mathrm{err}_{r,N}(M) < 10^{-3}$ in all the cases examined. Moreover, $\mathrm{err}_{r,N}(M) < 10^{-4}$ is achieved for $M = 40$ in all the cases examined. In figure 3*b*, the plane wave impinges onto the disk surface at the grazing incidence ($\theta_0 = 90°, \phi_0 = 0°$) with TE polarization. As can be clearly seen, the convergence rate is substantially not affected by the incidence angle. Indeed, $M = 20, 40$ allow to obtain again $\mathrm{err}_{e,N}(M) < 10^{-3}, 10^{-4}$, respectively, in all the cases examined. For the sake of completeness, it is worth observing that the proposed method is very efficient even in terms of computation time. Indeed, a few seconds are needed to reconstruct the solution by means of an in-house software code running on a laptop equipped with an Intel Core i7–10510U 1.8 GHz, 16 GB RAM.

(b) Normal incidence

In order to validate the GBC model, i.e. the replacement of a finite-thickness graphene-covered disk with its zero-thickness counterpart, in figure 4, the frequency dependence of ACS for such a model with $\varepsilon_r = 1$ and $\mu_c = 1$ eV is compared, for normal incidence, with ACS of two stacked graphene disks, with distance τ between them and the same other parameters, analysed using the full-wave guaranteed-convergence method proposed in [38]. As can be clearly seen, the agreement is very good across the entire frequency range considered.

The next step is the analysis of the resonance behaviour of the GDG disk in the THz range. Each resonance is caused by some natural mode of the scatterer, and their frequencies can be identified by the peaks of TSCS and ACS. For this reason, in figure 5, TSCS and ACS of the GDG

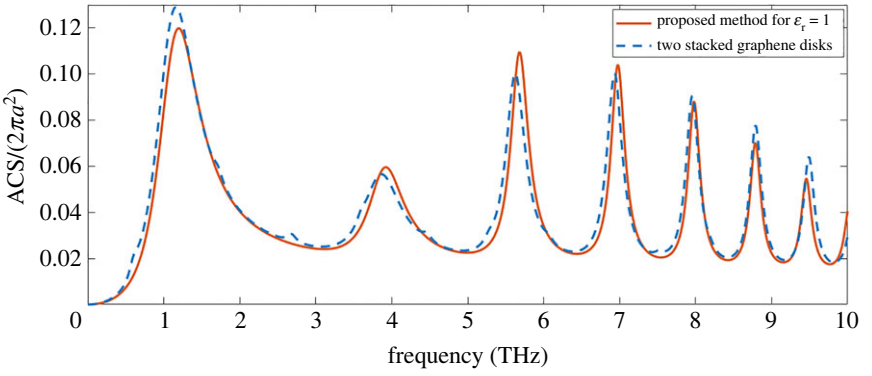

Figure 4. Normalized spectrum of ACS of the GDG disk with $\varepsilon_r = 1$, $\mu_r = 1$, $a = 50$ μm, $\tau = 0.04a$, $T = 300$ K, $t_{relax} = 1$ ps, $\mu_c = 1$ eV compared with ACS of two stacked graphene disks with distance τ between them, and the same radius, temperature, relaxation time and chemical potential, for normal incidence of the plane wave. (Online version in colour.)

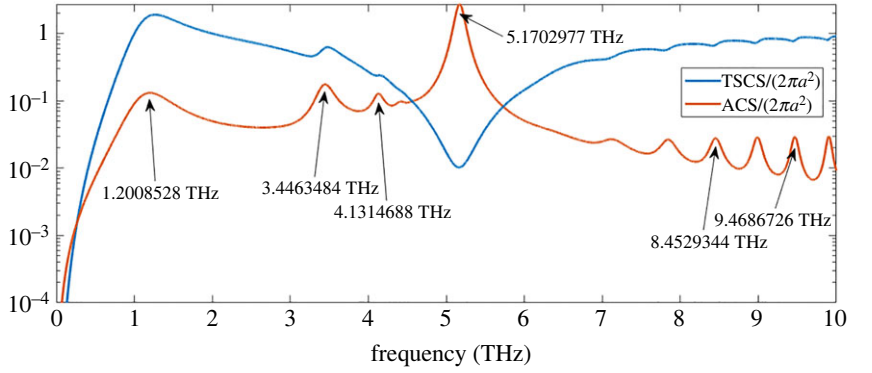

Figure 5. Normalized TSCS and ACS of the GDG disk with $\varepsilon_r = 12(1 - j10^{-5})$, $\mu_r = 1$, $a = 50$ μm, $\tau = 0.04a$, $T = 300$ K, $t_{relax} = 1$ ps, $\mu_c = 1$ eV, for varying values of the frequency and normal incidence. (Online version in colour.)

disk with the same parameters as in figure 3, are plotted for varying frequency, at the normal incidence, while, in figures 6–9, the resonances at the frequencies marked in figure 5 are studied.

The first, in frequency, resonance is seen at 1.2008528 THz, where the graphene impedance $|R''_e/Z_0|$ is relatively small, approximately thrice smaller than the free-space impedance (figure 2*a*), i.e. graphene is well conducting. It is worth observing that the corresponding peak of TSCS is at 1.2673490 THz (figure 6). The discrepancy between those two values results from the low Q-factor of this resonance. Inspection of the literature shows that such a resonance is observed even on a PEC disk as the first peak of TSCS [39], although shifted to 1.5081333 THz (figure 6). At this frequency, $ka = k_{11}a = 1.5804069$ that means $2a \approx \lambda/2$. Therefore, the corresponding mode is the 'half-wave dipole mode' of a PEC disk. Higher-order 'dipole' resonances can be seen at the frequencies corresponding to $2a \approx m\lambda/2$, where $m = 2,3, \ldots$ As expected, the Q-factors of these resonances are low: for the first one, it is above 1 but becomes even lower for the higher-order ones [39].

As can be seen in figure 6*a*, the curves, indeed, demonstrate that by increasing the chemical potential, which improves the conductivity, the behaviour of TSCS of the GDG disk approaches the same of the PEC disk. A confirmation of this interpretation is given by the behaviour of the total near electric field plotted in figure 6*b*,*c*, which is very small on the GDG disk surface except for the bright edge due to the singular edge behaviour of the electric field. Still, on the GDG disk,

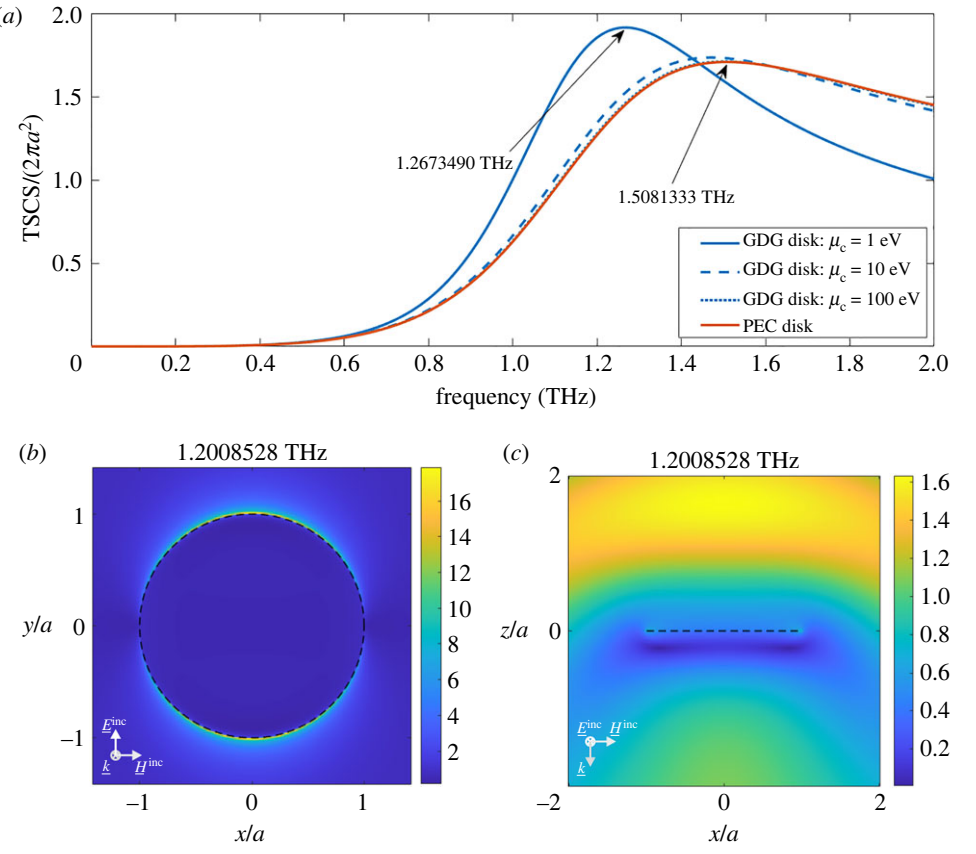

Figure 6. Normalized spectra of TSCS of the GDG disk with $\varepsilon_r = 12(1 - j10^{-5})$, $\mu_r = 1$, $a = 50$ μm, $\tau = 0.04a$, $T = 300$ K, $t_{relax} = 1$ ps, and three values of the chemical potential ($\mu_c = 1, 10, 100$ eV), compared with TSCS of a PEC disk with the same radius, for normal incidence (*a*), and total near electric field behaviour at the resonance frequency 1.2008528 THz for $\underline{E}_0 = 1\hat{y}$ V/m: E-field in the *xy*-plane (*b*) and E-field in the *xz*-plane (*c*). (Online version in colour.)

the lowest, in frequency, resonance can be also interpreted as the resonance on the lowest plasmon mode, P_{11}—see an approximate description of the circular plasmonic scatterers as Fabry–Perot resonators [40]. Note that, at the normal incidence, there are no other azimuthal harmonics except those with $n = \pm 1$, in the scattered field. Therefore, the whispering-gallery-like modes with $n \gg 1$ cannot be excited—they need oblique plane wave incidence.

The physical meaning of the resonances at 3.4463484 and 4.1314688 THz in figure 5 is explained in figure 7—they correspond to the plasmon modes P_{12} and P_{13} (figure 7*b–e*). In figure 7*a*, ACS of the considered GDG disk is compared with the one of a GDG disk obtained by substituting the dielectric material with air, which, as clearly shown in figure 4, works like two stacked graphene disks in the considered range of frequencies. Thus, the plasmon-mode resonances, P_{1m}, typical of the graphene disk [21], are excited on the considered GDG disk as well. However, their resonance frequencies are down-shifted due to the dielectric material between the graphene disks; the smallest shift is observed for the lowest in frequency 'quasi-PEC' plasmon mode P_{11}, apparently because of small $|R''_e/Z_0|$ values. This mode can be still called the 'half-wave dipole mode', however, now in terms of the wavelength of the hybrid plasmon guided wave of the pair of graphene monolayers. Then, the approximate characteristic equation is $J'_m(g_{plas}a) = 0$, where g_{plas} is the propagation constant of that wave and $J'_m(\cdot)$ is the derivative of the Bessel function of the first kind and order m.

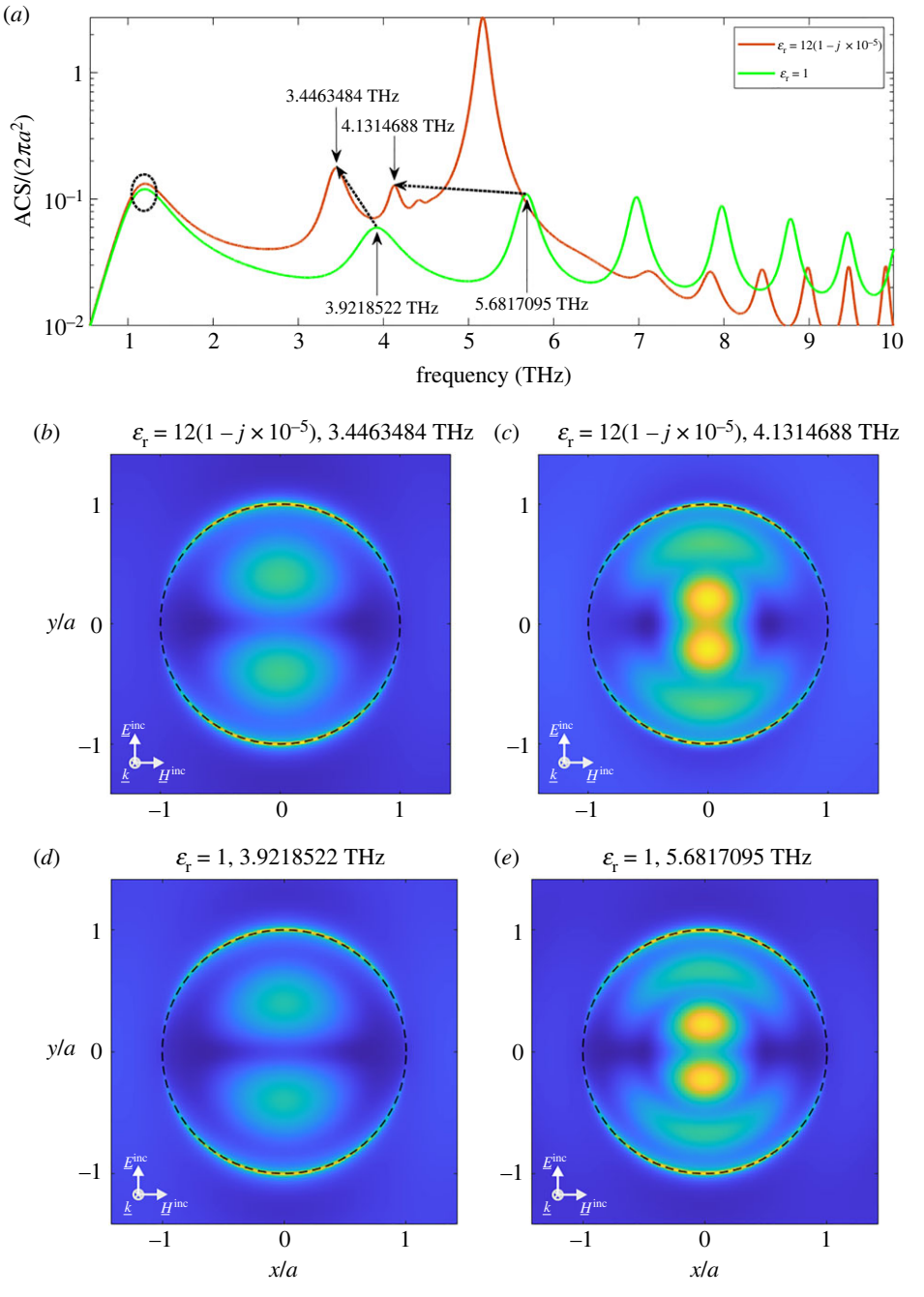

Figure 7. Normalized ACS of the GDG disk with $\varepsilon_r = 12(1 - j10^{-5})$, $\mu_r = 1$, $a = 50$ μm, $\tau = 0.04a$, $T = 300$ K, $t_{relax} = 1$ ps, $\mu_c = 1$ eV, compared with the one of a GDG disk obtained by substituting the dielectric material with air ($\varepsilon_r = 1$), for varying frequency and normal incidence (*a*), and total near electric field behaviour in the *xy*-plane at two plasmon-mode resonance frequencies for both the disk configurations and for $\underline{E}_0 = 1\hat{y}$ V/m: E-field for $\varepsilon_r = 12(1 - j10^{-5})$ at 3.4463484 THz (*b*), E-field for $\varepsilon_r = 12(1 - j10^{-5})$ at 4.1314688 THz (*c*), E-field for $\varepsilon_r = 1$ at 3.9218522 THz (*d*) and E-field for $\varepsilon_r = 1$ at 5.5817095 THz (*e*). (Online version in colour.)

The resonance at 5.1702977 THz, showing a maximum of ACS, corresponding to a minimum of TSCS (figure 5), has a different nature—it can be called transverse-mode resonance because it is associated with the lowest mode of the infinite GDG slab, S_0. This conclusion is justified by the

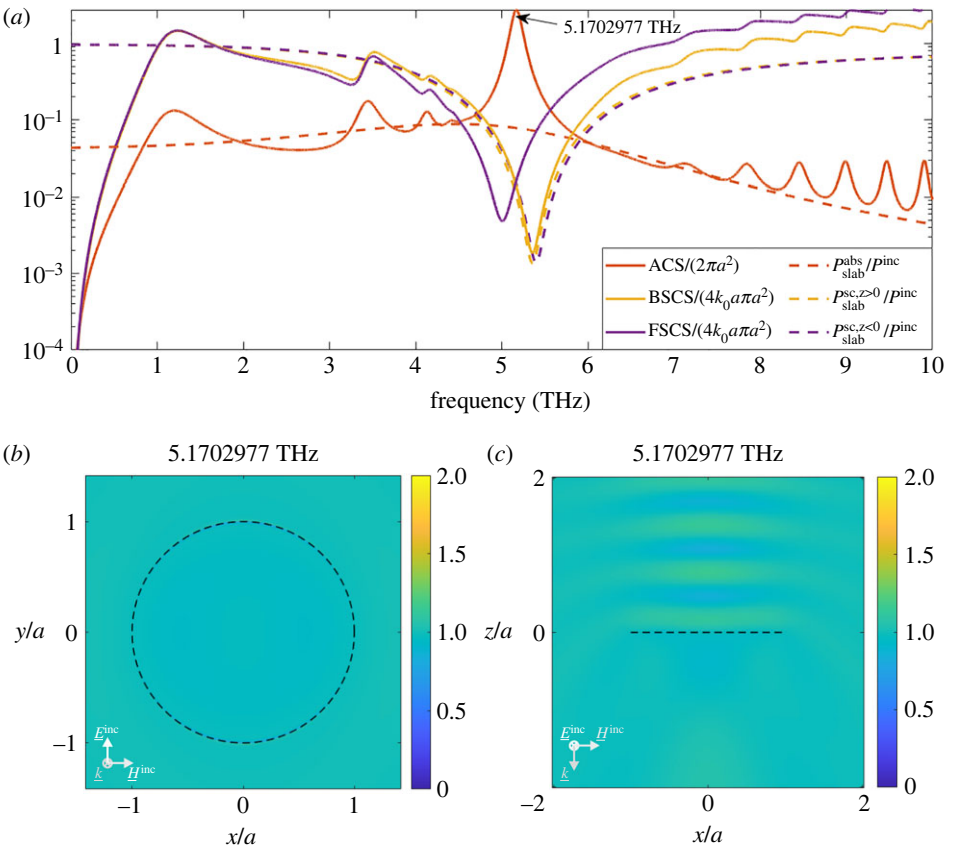

Figure 8. Normalized spectra of ACS, BSCS and FSCS of the GDG disk with $\varepsilon_r = 12(1 - j10^{-5})$, $\mu_r = 1$, $a = 50$ µm, $\tau = 0.04a$, $T = 300$ K, $t_{relax} = 1$ ps, $\mu_c = 1$ eV, compared, respectively, with the normalized (to the incidence power) power absorbed, scattered into the upper half-space and scattered into the lower half-space from a GDG slab with the same other parameters as the GDG disk, for normal incidence (*a*), and total near electric field behaviour at the resonance frequency 5.1702977 THz for $\underline{E}_0 = 1\hat{y}$ V/m in the *xy*-plane (*b*), and in the *xz*-plane (*c*). (Online version in colour.)

plots in figure 2*b*. Indeed, when replacing a 'thick' disk with a zero-thickness one with GBC on the former's median section, the thickness goes to the coefficients of GBC via the equations (2.1*a*) and (2.1*b*). As a result, the electric resistivity of the GDG composite has a peak, which is located at 5.1702977 THz if $\mu_c = 1$ eV—this peak then transfers into the peaks of TSCS and ACS.

This interpretation is also supported by the plots in figure 8*a*, where ACS, the back-scattering cross section (BSCS) and the forward-scattering cross section (FSCS) of the considered GDG disk are compared, respectively, with the normalized (to the incidence power) power absorbed (P^{abs}_{slab}/P^{inc}), scattered into the upper half-space ($P^{sc,z>0}_{slab}/P^{inc}$) and scattered into the lower half-space ($P^{sc,z<0}_{slab}/P^{inc}$) from a GDG slab with the same thickness, graphene covers and dielectric filler. As clearly shown in figure 8*b*,*c*, at this resonance frequency, the amplitude of the near total electric field is around 1 V/m. Hence, the total field is dominated by the incidence field, i.e. an almost total transparency can be observed.

Figure 9 clarifies the physical meaning of the resonances at 8.4529344 and 9.4686726 THz marked in figure 4—they correspond to the dipole-type dielectric disk modes, $H_{6,1,0}$ and $H_{8,1,0}$, respectively, slightly perturbed by the graphene covers. Here, the first subscript is related to the radial variation of the field, while the second one and third one take into account the azimuthal and transversal variations, respectively. In figure 9*a*, ACS is provided for the considered GDG disk and for a dielectric disk obtained by removing the graphene covers from the GDG disk

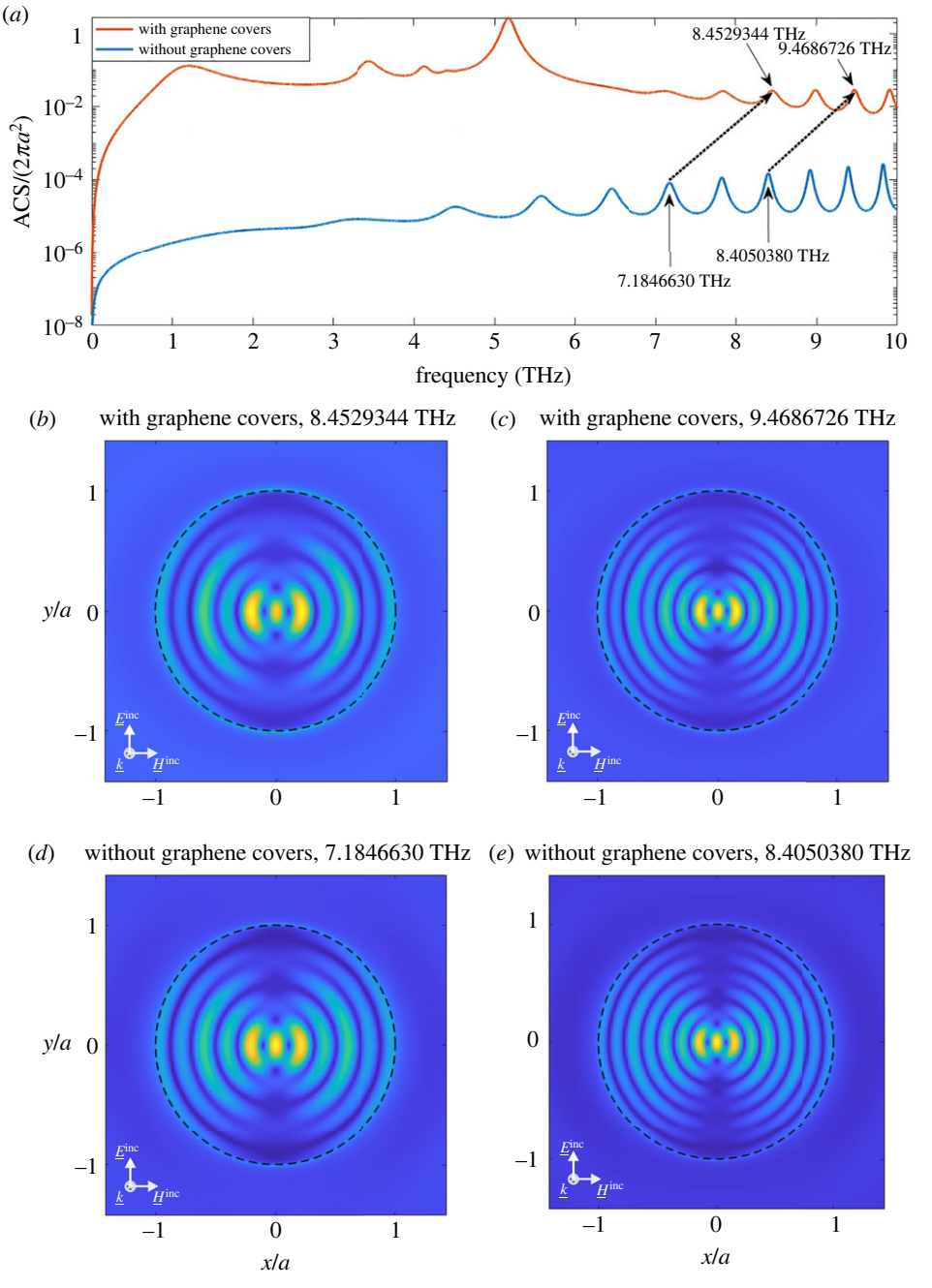

Figure 9. Normalized ACS of the GDG disk with $\varepsilon_r = 12(1 - j10^{-5})$, $\mu_r = 1$, $a = 50$ µm, $\tau = 0.04a$, $T = 300$ K, $t_{relax} = 1$ ps, $\mu_c = 1$ eV, compared with the one of a dielectric disk obtained by removing the graphene covers from the GDG disk, for varying values of the frequency and normal incidence (*a*), and total near electric field behaviour in the *xy*-plane at two dipole-mode resonance frequencies for both the disk configurations and for $\underline{E}_0 = 1\hat{y}$ V/m: E-field of the GDG disk at 8.4529344 THz (*b*), E-field of the GDG disk at 9.4686726THz (*c*), E-field of the dielectric disk at 7.1846630 THz (*d*), and E-field of the dielectric disk at 8.4050380 THz (*e*). (Online version in colour.)

itself. As clearly shown in figure 9*b–e*, the modes on the GDG disk resemble the classical dipole modes of the dielectric disk. In such a case, however, the resonance frequencies up-shift due to the graphene covers. It is interesting to observe that, for the plasmon-mode dipole-type resonances,

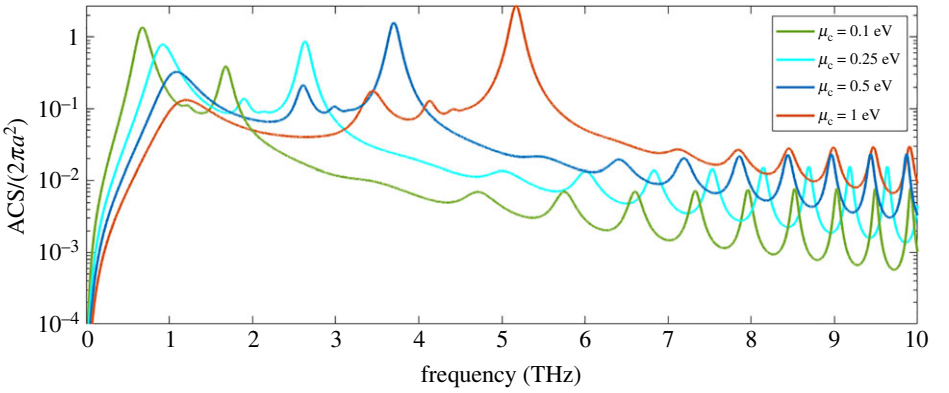

Figure 10. Normalized ACS of the GDG disk with $\varepsilon_r = 12(1 - j10^{-5})$, $\mu_r = 1$, $a = 50$ µm, $\tau = 0.04a$, $T = 300$ K, $t_{relax} =$ 1 ps and four values of the chemical potential ($\mu_c = 0.1, 0.25, 0.5, 1$ eV), versus the frequency at the normal incidence. (Online version in colour.)

the electric field spots develop along the incident electric field direction (figure 7*b–e*). While, for the dipole-type dielectric disk modes, the electric field spots are along the incident magnetic field direction.

Summarizing, at the normal incidence of the plane THz wave, the considered thin GDG disk is able to support the plasmon-mode dipole-type resonances, starting from the 'half-wave dipole' mode P_{11}, and the dielectric-mode dipole-type resonances, slightly perturbed by the presence of additional elements. Overlapping these resonances is the effect of quasi-full transparency related to the infinite slab mode resonance, S_0, incorporated into the GBC.

Now, we want to show that the resonance frequencies of all these modes can be tuned by changing the chemical potential. In figure 10, ACS of the GDG disk with $\varepsilon_r = 12(1 - j10^{-5})$ is plotted for four values of the chemical potential ($\mu_c = 0.1, 0.25, 0.5, 1$ eV) and for varying values of the frequency and normal incidence. As can be clearly seen, the resonance frequencies up-shift by increasing the chemical potential.

(c) Grazing incidence

At the oblique or grazing incidence of the plane wave, all azimuthal harmonics are present in the scattered field. This entails important changes in the spectral dependences of TSCS and ACS of the GDG disk because the resonances on the modes of higher azimuthal orders ($n > 1$) can be excited, with their frequencies tunable by changing the chemical potential. Such resonances, in principle, have larger Q-factors and hence can be more interesting in applications related to sensing and filtering.

To support this anticipation, in figure 11*a*,*b*, a comparison is shown between TSCS and ACS, respectively, of the GDG disk with $\varepsilon_r = 12(1 - j10^{-5})$ and two values of the chemical potential ($\mu_c = 0.01, 0.1$ eV), and a dielectric disk obtained by removing the graphene covers from the GDG disk itself, when a plane wave impinges onto the disk surface at the grazing incidence ($\theta_0 = 90°, \phi_0 = 0°$) with TE polarization and $\underline{E}_0 = 1\hat{y}$ V/m. Even in such a case, the resonance frequencies up-shift by introducing the graphene disks and by increasing the chemical potential. Indeed, for the marked frequencies, the total near electric field plotted in figure 11*c–h*, shows the same WGM-like behaviour. It is interesting to observe that the peaks become weaker if the chemical potential gets higher. This can be directly associated with a larger conductivity and hence a smaller impedance of the graphene covers. This entails the reduction of the electric field values at these covers, that is badly compatible with the plane wave field at the grazing incidence. As a result, the excitation efficiency of such WGM-like modes reduces at higher chemical potential

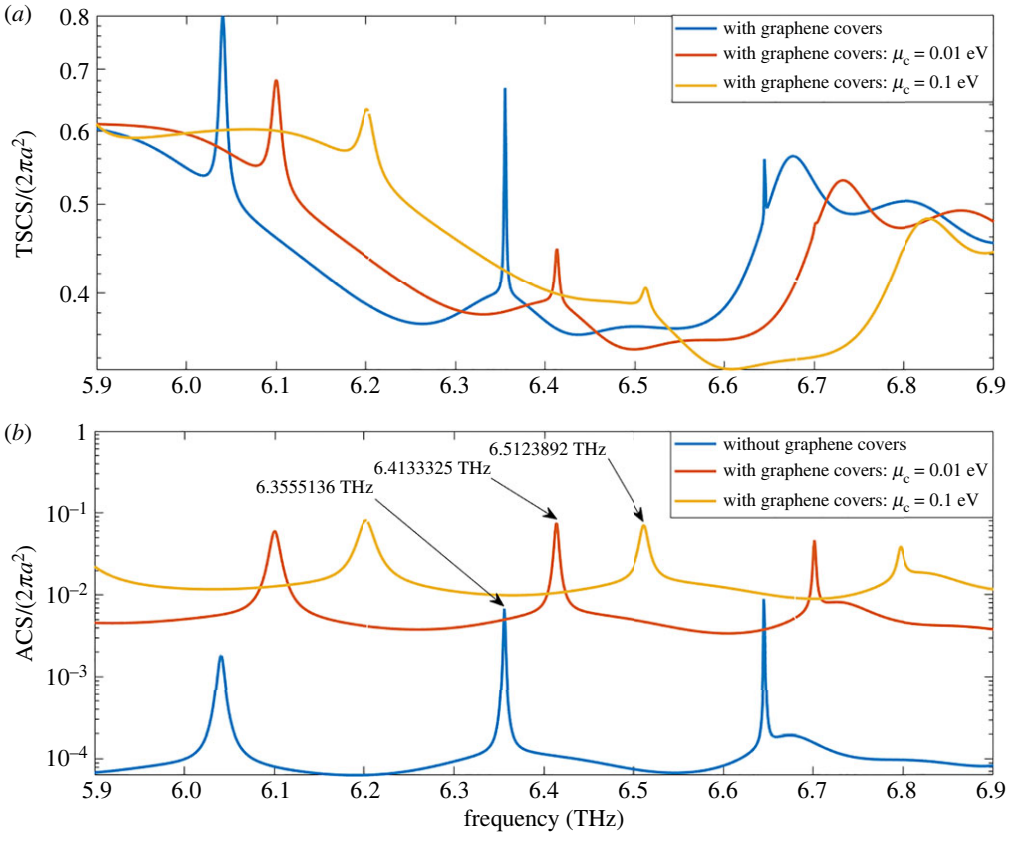

Figure 11. Normalized TSCS (*a*) and ACS (*b*) of the GDG disk with $\varepsilon_r = 12(1 - j10^{-5})$, $\mu_r = 1$, $a = 50$ µm, $\tau = 0.04a$, $T = 300$ K, $t_{relax} = 1$ ps and two values of the chemical potential ($\mu_c = 0.01, 0.1$ eV), compared with the ones of a dielectric disk obtained by removing the graphene covers from the GDG disk, for varying values of the frequency and grazing incidence ($\theta_0 = 90^\circ, \phi_0 = 0^\circ$) with TE polarization, and total near electric field behaviour at the marked resonance frequencies for $\underline{E}_0 = 1\hat{y}$ V/m: E-field in the *xy*-plane at the WGM resonance frequency 6.3555136 THz of the dielectric disk (*c*), E-field in the *xz*-plane at the WGM resonance frequency 6.3555136 THz of the dielectric disk (*d*), E-field in the *xy*-plane at the WGM resonance frequency 6.4133325 THz of the GDG disk with $\mu_c = 0.01$ eV (*e*), E-field in the *xz*-plane at the WGM resonance frequency 6.4133325 THz of the GDG disk with $\mu_c = 0.01$ eV (*f*), E-field in the *xy*-plane at the WGM resonance frequency 6.5123892 THz of the GDG disk with $\mu_c = 0.1$ eV (*g*), and E-field in the *xz*-plane at the WGM resonance frequency 6.5123892 THz of the GDG disk with $\mu_c = 0.1$ eV (*h*). (Online version in colour.)

values. Note that potentials, higher than 1 eV, have not yet been reported in publications even for the best CVD samples.

For the sake of completeness, it is worth noting that, except for the transverse or slab mode resonances, no other ones are observed at the grazing incidence for the TM polarization, i.e. if the incident electric field is along the disk axis.

4. Conclusion

We have presented the model of the scattering and absorption of a plane electromagnetic wave by a composite graphene–dielectric–graphene disk of small thickness. This model is based on the reduction of the complexity of the problem, without the sacrificing of its three-dimensional nature, with the aid of the shrinking of the disk thickness to zero but imposing the generalized two-side boundary conditions of the resistive type. Here, the electric and magnetic resistivities

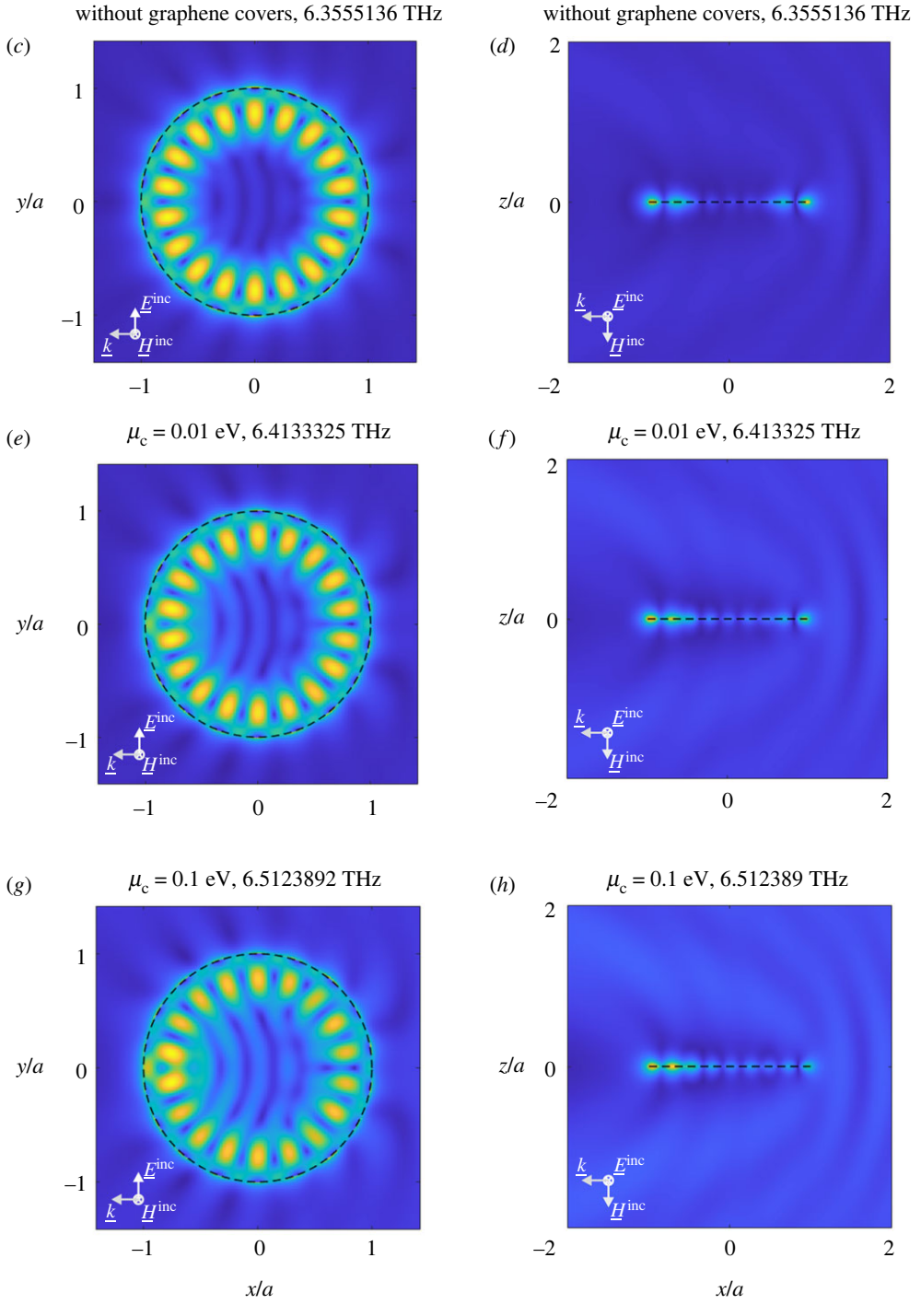

Figure 11. (*Continued.*)

serve as coefficients and inherit the original thickness and dielectric permittivity of the filler material. Then, an efficient numerical scheme, earlier developed for the scattering from PEC, resistive (for instance, graphene), and dielectric disks can be applied, modified for the presence of two graphene covers. It is based on the analytical preconditioning, i.e. the Galerkin projection

of the associated singular integral equations for the effective electric and magnetic currents on the sets of orthogonal polynomials, which are the eigenfunctions of the most singular parts of the operators involved. The code, based on such a scheme, is pointwise convergent as follows from the Fredholm theorems.

Numerical analysis of the plane wave scattering and absorption by such a composite scatterer shows that it behaves as a complicated open resonator, able to support natural modes of two types: graphene disk plasmon modes, slightly distorted by the presence of the dielectric disk filler and dielectric disk modes, slightly distorted by the graphene covers. All natural mode frequencies can be efficiently tuned by varying the graphene chemical potential.

Additionally, the scattering analysis reveals the alternating regimes of damped reflection (i.e. quasi-full transparency) or enhanced reflection near the frequencies of the natural modes of the infinite layer of the same composition. The latter effect has been earlier observed in the scattering from a bare dielectric disk. Due to the presence of graphene covers, in the case studied here its frequency becomes tunable as well.

Among future perspectives, the presented technique will be generalized to exploit the resonance behaviour and the tunability of composite disks involving graphene and dielectric disks with different characteristics. The generalization is straightforward for symmetric with respect to the median surface S structures, requiring only the adaptation of the effective resistivities. In the more general case of non-symmetric structures, the problem can be simply approached by considering even the cross-resistivity relating the effective electric and magnetic currents in the equations (2.5*a*) and (2.5*b*).

Data accessibility. The data presented in this study have been obtained by means of an in-house software code implementing the proposed method.

Authors' contributions. M.L.: conceptualization, data curation, formal analysis, funding acquisition, investigation, methodology, project administration, resources, software, validation, visualization, writing—original draft, writing—review and editing; M.V.B.: data curation, software, validation, visualization; A.I.N.: conceptualization, formal analysis, funding acquisition, investigation, methodology, project administration, resources, supervision, visualization, writing—original draft, writing—review and editing.

All authors gave final approval for publication and agreed to be held accountable for the work performed therein.

Conflict of interest declaration. We declare we have no competing interests.

Funding. This work was supported, in part, by the Italian Ministry of University Program 'Dipartimenti di Eccellenza 2018–2022', the National Research Foundation of Ukraine, grant no. 2020-01-0150 and the National Academy of Sciences of Ukraine, project no. 6541230-77-2022.

References

1. Garcia de Abajo FJ. 2014 Graphene plasmonics: challenges and opportunities. *ACS Photonics* **1**, 135–152. (doi:10.1021/ph400147y)
2. Low T, Avouris P. 2014 Graphene plasmonics for terahertz to mid-infrared applications. *ACS Nano* **8**, 1086–1101. (doi:10.1021/nn406627u)
3. Ullah Z, Witjaksono G, Nawi I, Tansu N, Khattak M, Junaid M. 2020 A review on the development of tunable graphene nanoantennas for terahertz optoelectronic and plasmonic applications. *Sensors* **20**, 1401. (doi:10.3390/s20051401)
4. Hanson GW. 2008 Dyadic Green's functions and guided surface waves for a surface conductivity model of graphene. *J. Appl. Phys.* **103**, 064302. (doi:10.1063/1.2891452)
5. Rodrigo D, Limaj O, Janner D, Etezadi D, Abajo F, Pruneri V, Altug H. 2015 Mid-infrared plasmonic biosensing with graphene. *Science* **349**, 165–168. (doi:10.1126/science.aab2051)
6. Mencarelli D, Nishina Y, Ishikawa A, Pierantoni L, Bellucci S. 2017 THz plasmonic resonances in hybrid reduced-graphene-oxide and graphene patterns for sensing applications. *Opt. Data Process. Storage* **3**, 89–96. (doi:10.1515/odps-2017-0011)
7. Nag A, Mitra A, Mukhopadhyay SC. 2018 Graphene and its sensor-based applications: a review. *Sens. Actuator A Phys.* **270**, 177–194. (doi:10.1016/j.sna.2017.12.028)

8. Fuscaldo W, Burghignoli P, Baccarelli P, Galli A. 2017 Efficient 2-D leaky-wave antenna configurations based on graphene metasurfaces. *Int. J. Microw. Wirel. Technol.* **9**, 1293–1303. (doi:10.1017/S1759078717000459)
9. Prelat L, Cuevas M, Passarelli N, Bustos Marun R, Depine R. 2021 Spaser and optical amplification conditions in graphene-coated active wires. *J. Opt. Soc. Am. B* **38**, 2118–2126. (doi:10.1364/JOSAB.423734)
10. Du X, Skachko I, Barker A, Andrei EY. 2008 Approaching ballistic transport in suspended graphene. *Nat. Immunol.* **3**, 491–495. (doi:10.1038/nnano.2008.199)
11. Banszerus L*et al.* 2015 Ultrahigh-mobility graphene devices from chemical vapor deposition on reusable copper. *Sci. Adv.* **1**, e1500222. (doi:10.1126/sciadv.1500222)
12. Čtyroký J, Petráček J, Kwiecien P, Richter I, Kuzmiak V. 2020 Graphene on an optical waveguide: comparison of simulation approaches. *Opt. Quantum Electron.* **52**, 149. (doi:10.1007/s11082-020-02265-0)
13. Niu K, Li P, Huang Z, Jiang LJ, Bagci H. 2020 Numerical methods for electromagnetic modeling of graphene: a review. *IEEE J. Multiscale Multiphys. Comput. Tech.* **5**, 44–58. (doi:10.1109/JMMCT.2020.2983336)
14. Lucido M, Kobayashi K, Medina F, Nosich AI, Vinogradova ED. 2021 Guest editorial: method of analytical regularisation for new frontiers of applied electromagnetics. *IET Microw. Antennas Propag.* **15**, 1127–1132. (doi:10.1049/mia2.12182)
15. Balaban MV, Smotrova EI, Shapoval OV, Bulygin VS, Nosich AI. 2012 Nystrom-type techniques for solving electromagnetics integral equations with smooth and singular kernels. *Int. J. Numer. Model Electron. Netw. Devices Fields* **25**, 490–511. (doi:10.1002/jnm.1827)
16. Zinenko TL, Matsushima A, Nosich AI. 2020 Terahertz range resonances of metasurface based on double grating of microsize graphene strips inside dielectric slab. *Proc. R. Soc. A* **476**, 20200173. (doi:10.1098/rspa.2020.0173)
17. Yevtushenko FO, Dukhopelnykov SV, Zinenko TL, Rapoport YG. 2021 Electromagnetic characterisation of tuneable graphene-strips-on-substrate metasurface in the whole THz range: analytical regularization and interplay of natural-mode resonances. *IET Microw. Antennas Propag.* **15**, 1225–1239. (doi:10.1049/mia2.12158)
18. Shapoval OV, Nosich AI. 2016 Bulk refractive-index sensitivities of the THz-range plasmon resonances on a micro-size graphene strip. *J. Phys. D: Appl. Phys.* **49**, 055105. (doi:10.1088/0022-3727/49/5/055105)
19. Kaliberda ME, Lytvynenko LM, Pogarsky SA. 2018 Modeling of graphene planar grating in the THz range by the method of singular integral equations. *Frequenz* **72**, 277–284. (doi:10.1515/freq-2017-0059)
20. Balaban MV, Shapoval OV, Nosich AI. 2013 THz wave scattering by a graphene strip and a disk in the free space: integral equation analysis and surface plasmon resonances. *J. Optics* **15**, 114007. (doi:10.1088/2040-8978/15/11/114007)
21. Lucido M. 2021 Electromagnetic scattering from a graphene disk: Helmholtz-Galerkin technique and surface plasmon resonances. *Mathematics* **9**, 1429. (doi:10.3390/math9121429)
22. Bulygin VS, Nosich AI, Gandel YV. 2012 Nystrom-type method in three-dimensional electromagnetic diffraction by a finite PEC rotationally symmetric surface. *IEEE Trans. Antennas Propag.* **60**, 4710–4718. (doi:10.1109/TAP.2012.2209194)
23. Saidoglu NY, Nosich AI. 2020 Method of analytical regularization in the analysis of axially symmetric excitation of imperfect circular disk antennas. *Comput. Math. Appl.* **79**, 2872–2884. (doi:10.1016/j.camwa.2019.12.020)
24. Bleszynski E, Bleszynski M, Jaroszewicz T. 1993 Surface-integral equations for electromagnetic scattering from impenetrable and penetrable sheets. *IEEE Antennas Propag. Mag.* **35**, 14–24. (doi:10.1109/74.248480)
25. Karlsson A. 2009 Approximate boundary conditions for thin structures. *IEEE Trans. Antennas Propag.* **57**, 144–148. (doi:10.1109/TAP.2008.2009720)
26. Balaban MV. 2015 *Modeling of stratified graphene-dielectric structures using the generalized boundary conditions: THz wave scattering by a thin sandwiched disk*. In *Proc. Int. Conf. Electronics and Nanotechnology (ELNANO-2015), Kyiv, Ukraine, 21–24 April*, pp. 89–92. Institute of Electrical and Electronics Engineers (IEEE).
27. Lucido M, Balaban MV, Dukhopelnykov SV, Nosich AI. 2020 A fast-converging scheme for the electromagnetic scattering from a thin dielectric disk. *Electronics* **9**, 1451. (doi:10.3390/electronics9091451)

28. Lucido M, Balaban MV, Nosich AI. 2021 Plane wave scattering from thin dielectric disk in free space: generalized boundary conditions, regularizing Galerkin technique and whispering gallery mode resonances. *IET Microw. Antennas Propag.* **15**, 1159–1170. (doi:10.1049/mia2.12106)
29. Han MY, Oezyilmaz B, Zhang Y, Kim P. 2007 Energy band gap engineering of graphene nanoribbons. *Phys. Rev. Lett.* **98**, 206805. (doi:10.1103/PhysRevLett.98.206805)
30. Oguzer T, Altintas A. 2021 E-polarization THz-range focusing of microsize parabolic reflector with graphene-sandwiched thin dielectric layer. *IET Microw. Antennas Propag.* **15**, 1240–1248. (doi:10.1049/mia2.12161)
31. Jones DS. 1964 *The theory of electromagnetism*. New York, NY: Pergamon Press.
32. Chew WC, Kong JA. 1980 Resonance of nonaxial symmetric modes in circular microstrip disk antenna. *J. Math. Phys.* **21**, 2590–2598. (doi:10.1063/1.524366)
33. Lucido M, Panariello G, Schettino F. 2017 Scattering by a zero-thickness PEC disk: a new analytically regularizing procedure based on Helmholtz decomposition and Galerkin method. *Radio Sci.* **52**, 2–14. (doi:10.1002/2016RS006140)
34. Lucido M, Di Murro F, Panariello G. 2017 Electromagnetic scattering from a zero-thickness PEC disk: a note on the Helmholtz-Galerkin analytically regularizing procedure. *Prog. Electromagn. Res. Lett.* **71**, 7–13. (doi:10.2528/PIERL17072006)
35. Lucido M, Schettino F, Panariello G. 2021 Scattering from a thin resistive disk: a guaranteed fast convergence technique. *IEEE Trans. Antennas Propag.* **69**, 387–396. (doi:10.1109/TAP.2020.3008643)
36. Van Bladel J. 1993 A discussion of Helmholtz' theorem on a surface. *AEÜ* **47**, 131–136.
37. Geng N, Carin L. 1999 Wide-band electromagnetic scattering from a dielectric BOR buried in a layered lossy dispersive medium. *IEEE Trans. Antennas Propag.* **47**, 610–619. (doi:10.1109/8.768799)
38. Lucido M. 2021 Analysis of the scattering from a two stacked thin resistive disks resonator by means of the Helmholtz–Galerkin regularizing technique. *Appl. Sci.* **11**, 8173. (doi:10.3390/app11178173)
39. Bowman JJ, Senior TBA, Uslenghi PLE. 1970 *Electromagnetic and acoustic scattering by simple shapes*. Amsterdam, The Netherlands: North-Holland Pub. Co.
40. Filter R, Qi J, Rockstuhl C, Lederer F. 2012 Circular optical nanoantennas: an analytical theory. *Phys. Rev. B* **85**, 125429. (doi:10.1103/PhysRevB.85.125429)